



# Multi-scale modeling of the macroscopic, elastic mismatch and thermal misfit stresses in metal matrix composites



X.X. Zhang<sup>a</sup>, B.L. Xiao<sup>a</sup>, H. Andrä<sup>b</sup>, Z.Y. Ma<sup>a,\*</sup>

<sup>a</sup>Shenyang National Laboratory for Materials Science, Institute of Metal Research, Chinese Academy of Sciences, 72 Wenhua Road, Shenyang 110016, China

<sup>b</sup>Fraunhofer Institute for Industrial Mathematics, Fraunhofer-Platz 1, Kaiserslautern 67663, Germany

## ARTICLE INFO

### Article history:

Available online 12 February 2015

### Keywords:

Multiscale modeling  
Metal matrix composites  
Heterogeneous materials  
Residual stress  
Finite element analysis

## ABSTRACT

A 3D multiscale method is proposed to model the residual stresses in multiphase materials under the hybrid-semiconcurrent multiscale framework. As an illustration, the quenching residual stresses in SiC<sub>p</sub>/2124Al composite are modeled. The total residual stresses are separated into the macro, elastic misfit and thermal misfit residual stresses by means of the present multiscale model. In this multiscale model, one macroscale model is connected to two microscale models via scale transition boundary conditions. The predicted total residual strains in the metal matrix and the reinforcing particles coincide with reported experimental data very well. The predicted total, macro, elastic misfit and thermal misfit residual stresses agree reasonably well with the reported experimental ones. The present model provides a new tool to gain a deep insight into the residual stresses in multiphase materials.

© 2015 Elsevier Ltd. All rights reserved.

## 1. Introduction

Due to their outstanding properties, metal matrix composites (MMC) are widely used in advanced industries. Nonetheless, the residual stresses in MMC influence their mechanical behavior significantly [1–6]. To guarantee high-performance, reliability and safety, the distribution and magnitude of residual stress should be controlled. The corresponding initial and crucial step is to obtain an accurate knowledge of the residual stresses. Unfortunately, both the measurement and prediction of residual stresses are historically difficult [7].

Residual stresses in MMC include the macro, elastic misfit and thermal misfit residual stresses, and are usually measured by means of the neutron or synchrotron X-ray diffraction. Different parts of the measured total residual stresses in each phase of MMC can be separated via the method proposed by Fitzpatrick et al. [8]. However, accurate measurement of the triaxial residual strains via the diffraction techniques encounters the problem that it is quite difficult to precisely measure the “stress free” lattice parameters  $d_0$  [8–10]. Other factors which influence the accuracy of measurement include the gauge volume effect [11], the grain size effect (involved in thermal neutron source method) [12] and the texture effect [12].

In order to investigate and control the residual stresses in MMC efficiently, advanced modeling and simulation methods are necessary. In the past two decades, much research has only focused on modeling the thermal misfit residual stresses via finite element method, for instance, see the works of Povirk et al. [13], Ho and Saingal [14], and Schmauder et al. [15]. These studies have shown that tensile thermal misfit residual stress remains in the metal matrix and compressive thermal misfit residual stress remains in the reinforcing particles. In addition, the influences of particle content, shape and arrangement on the thermal misfit residual stress was demonstrated by Bouafia et al. [16]. The influences of thermal misfit residual stress on the mechanical properties, such as the yield behavior [17] and damage mechanism [15] were also assessed. However, few studies have compared the predicted thermal misfit residual stress with the measured one. Furthermore, one important and fundamental issue in modeling the residual stresses in MMC is that there is still a lack of an efficient numerical algorithm to predict and further separate the macro, elastic misfit and thermal misfit residual stresses in MMC.

In recent years, much research has focused on development of multiscale modeling techniques of MMC [18]. For example, Ghosh et al. [19,20] used multiscale method by combining the asymptotic homogenization method with the Voronoi cell finite element method to investigate the elasto-plastic deformation and damage behaviors of heterogeneous (porous and composite) materials. Özdemir et al. [21] proposed a FE<sup>2</sup> multiscale method for the thermo-elastoplastic analysis of heterogeneous solids.

\* Corresponding author. Tel./fax: +86 24 83978908.  
E-mail address: [zyma@imr.ac.cn](mailto:zyma@imr.ac.cn) (Z.Y. Ma).

Residual stresses in MMC result from thermo-elastoplastic deformation. Therefore, in principle, it is possible to introduce multiscale method to study all parts of residual stresses in MMC. Such a spark of hope arose after the work of Golanski et al. [22] who modeled both the macro and micro thermal residual stresses in surface TaC/stellite and TiC/stellite composite layers via multiscale modeling method. This example indicates that the multiscale modeling method is a powerful tool to explore the residual stresses in composites. Unfortunately, this model only deals with elastic deformation and is not suitable for MMC. In many processes of MMC, such as heat treatment, material processing and friction stir welding, plastic deformation is an important phenomenon in the metal matrix. Hence, there remains a strong need to develop a new multiscale model to investigate the residual stresses in MMC.

The primary aim of this study is to present a multiscale model for predicting and separating the macro, elastic misfit and thermal misfit residual stresses in MMC. Besides the initial and boundary conditions, the multiscale model only takes the material properties of each phase as the input parameters. Temperature dependent material properties are taken into account. Both reinforcing particles and metal matrix are modeled as elasto-plastic materials. As an illustration of this multiscale model, a real process of a real material, i.e. the quenching process of the 3  $\mu\text{m}$  17 vol.% SiC<sub>p</sub>/2124Al composite, is studied.

## 2. The multiscale thermo-elastoplastic problem

Generally, the numerical multiscale methods can be classified into two basic types: concurrent and hierarchical [23,24]. In concurrent methods the macroscale and microscale models are strongly coupled together and solved simultaneously, while the hierarchical methods pre-compute the effective properties and use them to construct a macroscale model further. Besides these two basic methods, several methods fall in the spectrum between them, for example, the semiconcurrent method and the hybrid-semiconcurrent method [20,24–26].

A comparison between these methods with respect to the information transfer, the relative computational costs and scales where the final unknown fields are computed are listed in Table 1. In the present work, the hybrid-semiconcurrent multiscale method is employed where the semiconcurrent domain is defined by the interesting and important region.

### 2.1. Macroscale thermo-mechanical problem

At the macroscale, a bounded structure  $\Omega$  with the boundary  $\partial\Omega$  is considered. The governing heat equation at the macroscale is given by

$$\rho_M c_M \dot{T}_M - \nabla \cdot (k_M \nabla T_M) = 0 \quad \text{in } \Omega, \quad (1)$$

where subscript  $M$  denotes the macroscale,  $T$  the temperature,  $\rho$  the density,  $c$  the heat capacity,  $k$  the heat conductivity coefficient, the upper dot denotes the time derivative.

The initial temperature condition for the whole structure is

$$T_M|_{t=0} = T_0 \quad \text{in } \Omega, \quad (2)$$

where  $T_0$  is the initial temperature.

The convective heat transfer boundary condition for the heat exchange  $q_M$  is given by

$$q_M = h(T - T_a) \quad \text{on } \partial\Omega_c, \quad (3)$$

where  $h$  is the heat transfer coefficient,  $T_a$  is the environmental temperature.

The radiative heat transfer boundary condition for the heat exchange  $q_M$  is given by

$$q_M = A(T^4 - T_a^4) \quad \text{on } \partial\Omega_r, \quad (4)$$

where the factor  $A$  is the product of the emissivity factor times the Stefan-Boltzmann constant.

The quasi-static mechanical equilibrium equation within the infinitesimal deformation framework at the macroscale reads

$$\nabla \cdot \boldsymbol{\sigma}_M = 0 \quad \text{in } \Omega, \quad (5)$$

where  $\boldsymbol{\sigma}$  is the stress tensor.

The initial displacement condition at the macroscale is

$$\mathbf{u}_M|_{t=0} = \mathbf{0} \quad \text{on } \partial\Omega_u, \quad (6)$$

where  $\mathbf{u}$  is the displacement vector.

### 2.2. Microscale thermo-mechanical problem

For modeling the elastic misfit and thermal misfit residual stresses, a cubic unit cell  $\omega$  with the boundary  $\partial\omega$  is considered at the microscale. Homogeneous temperature distribution in the unit cell is assumed. Such a hypothesis is acceptable under the following conditions. The heat transfer ability of all phases in MMC should be good, for example in SiC/Al composites. On the other hand, the size of the unit cell is quite small. Furthermore, the temperature gradient at the macroscale is not extremely high. When these conditions are obeyed, the temperature  $T_m$  in the domain at the microscale are assumed to be equal to the temperature at the macroscale Gaussian integration point  $T_M^g$ . This means

$$T_m = T_M^g \quad \text{in } \omega, \quad (7)$$

where subscript  $m$  denotes the microscale and superscript  $g$  denotes the macroscale Gaussian integration point.

The quasi-static mechanical equilibrium equation within the infinitesimal deformation framework at the microscale reads

$$\nabla \cdot \boldsymbol{\sigma}_m = 0 \quad \text{in } \omega. \quad (8)$$

The initial displacement condition at the microscale is

$$\mathbf{u}_m|_{t=0} = \mathbf{0} \quad \text{in } \omega. \quad (9)$$

The kinematic uniform boundary conditions (KUBC) generally hold

$$\mathbf{u}_m = \boldsymbol{\varepsilon}_M^g \cdot \mathbf{x}_m \quad \text{on } \partial\omega_u, \quad (10)$$

where  $\boldsymbol{\varepsilon}_M^g$  is a macroscale strain tensor corresponding to the macroscale Gaussian integration point which is defined as the

**Table 1**  
Comparison between different multi-scale methods.

Methods	Information transfer [24]*	Relative computational costs	Scales, where the final unknown fields are computed
Concurrent	$\Omega^{\text{micro}} \leftrightarrow \Omega^{\text{macro}}$	High	Macro and micro
Hierarchical	$\Omega^{\text{micro}} \rightarrow \Omega^{\text{macro}}$	Low	Macro
Semiconcurrent	$\Omega^{\text{micro}} \leftrightarrow \Omega^{\text{macro}}$	Middle	Macro and micro
Hybrid-semiconcurrent	$\begin{cases} \Omega^{\text{micro}} \rightarrow \Omega^{\text{macro}}, & \text{in hierarchical domain} \\ \Omega^{\text{micro}} \leftrightarrow \Omega^{\text{macro}}, & \text{in semiconcurrent domain} \end{cases}$	Between hierarchical and semiconcurrent	Macro for whole domain, micro for semiconcurrent domain

\*  $\leftrightarrow$ : strong coupling;  $\rightarrow, \leftrightarrow$ : weak coupling.

macro–micro point in the present work,  $\mathbf{x}_m$  is the position of the boundary node. In the present work, two microscale models are constructed via different definitions of  $\boldsymbol{\varepsilon}_m^g$  in order to separate the macro, elastic misfit and thermal misfit residual stresses (see Section 2.5).

### 2.3. Microscale constitutive model

At the microscale, every phase in MMC is described by an infinitesimal thermo-elastoplastic constitutive model [27]. In this way, the model can handle the situations that plasticity occurs in both the reinforcing particles and the metal matrix. For rigid ceramic reinforcing particles that normally undergo only elastic deformation, the yield stress of them is then set as a large number near infinite (e.g.  $10^{15}$  MPa). The  $J_2$ -flow theory of thermo-elastoplasticity is adopted.

The total strain tensor is decomposed as

$$\boldsymbol{\varepsilon}_m^{total} = \boldsymbol{\varepsilon}_m^e + \boldsymbol{\varepsilon}_m^p + \boldsymbol{\varepsilon}_m^{th}, \quad (11)$$

where subscript  $m$  denotes the microscale, and superscript  $e$ ,  $p$  and  $th$  denote elastic, plastic and thermal, respectively. The thermal strain tensor is calculated by

$$\boldsymbol{\varepsilon}_m^{th} = \alpha \Delta T \mathbf{I}, \quad (12)$$

where  $\alpha$  is the coefficient of thermal expansion,  $\Delta T$  denotes the temperature variation,  $\mathbf{I}$  denotes the second order identity tensor.

The stress tensor is calculated via the Hooke's law

$$\boldsymbol{\sigma}_m = \mathbf{D}_m : \boldsymbol{\varepsilon}_m^e, \quad (13)$$

$$\mathbf{D}_m = \left[ \frac{E\nu}{(1+\nu)(1-2\nu)} \mathbf{I} \otimes \mathbf{I} + \frac{E}{1+\nu} \mathbf{I} \right], \quad (14)$$

where  $E$  is the Young's modulus,  $\nu$  is the Poisson's ratio,  $\mathbf{I}$  is the fourth order identity tensor.

The von-Mises yield function [27] is defined by

$$f_m(\boldsymbol{\sigma}_m, p_m) = \sqrt{3/2} \|dev(\boldsymbol{\sigma}_m)\| - \sigma_m(p_m), \quad (15)$$

where  $p$  indicates the accumulated plastic strain (APS),  $\|\bullet\|$  denotes the norm of the indicated tensor,  $dev(\bullet)$  denotes the deviator of the indicated tensor,  $\sqrt{3/2} \|dev(\boldsymbol{\sigma})\|$  denotes the von-Mises equivalent stress and  $\sigma(p_m)$  denotes the yield stress.

The Voce type isotropic hardening rule [28] is

$$\sigma_m(p_m) = \sigma_m^\infty + h_m p_m + (\sigma_m^0 - \sigma_m^\infty) \exp(-l_m p_m), \quad (16)$$

where  $\sigma^0$  is the initial yield strength,  $\sigma^\infty$  is the ultimate strength, both  $h$  and  $l$  are the material constants.

### 2.4. Macroscale constitutive model

At the macroscale, the MMC is regarded as a homogenized material and also described by a  $J_2$ -flow theory of thermo-elastoplasticity [27]. The effective constitutive model of MMC is constructed based on pre-computed effective properties via computational homogenizations. The determination of the effective properties including the CTE  $\langle \alpha \rangle$ , Young's modulus  $\langle E \rangle$ , Poisson's ratio  $\langle \nu \rangle$  and isotropic hardening function of MMC are described in detail in reference [29]. The pre-constructed effective constitutive model of the MMC is summarized:

$$\boldsymbol{\varepsilon}_M = \boldsymbol{\varepsilon}_M^{ep} + \boldsymbol{\varepsilon}_M^{th}, \quad (17)$$

$$\boldsymbol{\varepsilon}_M^{ep} = \boldsymbol{\varepsilon}_M^e + \boldsymbol{\varepsilon}_M^p, \quad (18)$$

$$\boldsymbol{\varepsilon}_M^{th} = \langle \alpha \rangle \Delta T \mathbf{I}, \quad (19)$$

$$\boldsymbol{\sigma}_M = \mathbf{D}_{eff} : \boldsymbol{\varepsilon}_M^e, \quad (20)$$

$$\langle \mathbf{D} \rangle = \left[ \frac{\langle E \rangle \langle \nu \rangle}{(1 + \langle \nu \rangle)(1 - 2\langle \nu \rangle)} \mathbf{I} \otimes \mathbf{I} + \frac{\langle E \rangle}{1 + \langle \nu \rangle} \mathbf{I} \right], \quad (21)$$

$$f_M(\boldsymbol{\sigma}_M, p_M) = \sqrt{3/2} \|dev(\boldsymbol{\sigma}_M)\| - \sigma_M(p_M), \quad (22)$$

where superscript  $ep$  denotes elasto-plastic,  $\langle \mathbf{D} \rangle$  denotes the fourth order effective elastic tensor,  $\sigma_M(p_M)$  is the isotropic hardening function which is an Akima spline interpolation function of  $\langle \sigma_{Mises} \rangle$  with respect to  $\langle p \rangle$  (see reference [29] for more details).

### 2.5. Separation of the residual stresses via different definitions of boundary condition

The total residual strain  $\boldsymbol{\varepsilon}^{total}$  in each phase  $i$  is the sum of the macro residual strain  $\boldsymbol{\varepsilon}_M^e$ , the elastic misfit residual strain  $\boldsymbol{\varepsilon}^{mE}$  and the thermal misfit residual strain  $\boldsymbol{\varepsilon}^{mT}$  [8].

$$\boldsymbol{\varepsilon}_i^{total} = \boldsymbol{\varepsilon}_M^e + \boldsymbol{\varepsilon}_i^{mE} + \boldsymbol{\varepsilon}_i^{mT}. \quad (23)$$

Similarly, the corresponding total residual stress  $\boldsymbol{\sigma}^{total}$  in each phase  $i$  is the sum of the macro residual stress  $\boldsymbol{\sigma}_M$ , the elastic misfit residual stress  $\boldsymbol{\sigma}^{mE}$  and the thermal misfit residual stress  $\boldsymbol{\sigma}^{mT}$  [8].

$$\boldsymbol{\sigma}_i^{total} = \boldsymbol{\sigma}_M + \boldsymbol{\sigma}_i^{mE} + \boldsymbol{\sigma}_i^{mT}. \quad (24)$$

It should be noted here that the elastic misfit residual stress is the load transfer of the macro residual stress from one phase to another. Therefore, the elastic misfit residual stress is generated due to the inner cause that the elastic properties of the metal matrix differ from those of the reinforcing particles.

From this point of view, the macro and elastic misfit residual stresses should be grouped together due to the same external cause which is the inhomogeneous macroscale deformation. This inhomogeneous macroscale deformation is measured by the macroscale elasto-plastic strain  $\boldsymbol{\varepsilon}_M^{ep}$ . In order to compute the macro and elastic misfit residual stresses, the boundary condition of the microscale model I is constructed by

$$\mathbf{u}_m^I = \boldsymbol{\varepsilon}_M^{ep} \cdot \mathbf{x}_m. \quad (25)$$

Using this boundary condition, the microscale model I computes the residual stress field which is the sum of the macro and elastic misfit residual stresses, i.e.  $\boldsymbol{\sigma}_M + \boldsymbol{\sigma}_i^{mE}$ , from which the homogenized macro and elastic misfit residual stresses  $\langle \boldsymbol{\sigma}_M + \boldsymbol{\sigma}_i^{mE} \rangle$  in phase  $i$  over the microscale domain (e.g. a unit cell) can be computed via the homogenization function. A homogenized stress  $\langle \boldsymbol{\sigma} \rangle$  is useful because it reflects the stress averaged over the microscale domain and is comparable to a measured stress in a gauge volume via neutron diffraction measurement.

The elastic misfit residual stress  $\boldsymbol{\sigma}_i^{mE}$  is a kind of micro stress (also is referred to as type II stress), the microscale stress equilibrium of  $\boldsymbol{\sigma}_i^{mE}$  over the microscale domain equals to zero.

$$V \langle \boldsymbol{\sigma}_{pa}^{mE} \rangle + (1 - V) \langle \boldsymbol{\sigma}_{ma}^{mE} \rangle = 0, \quad (26)$$

where  $V$  denotes the volume fraction of reinforcing particles, subscripts  $pa$  and  $ma$  denote reinforcing particles and metal matrix.

The mixture of the homogenized macro and elastic misfit residual stresses equals to the macro residual stress  $\boldsymbol{\sigma}_M$ .

$$\boldsymbol{\sigma}_M = V \langle \boldsymbol{\sigma}_M + \boldsymbol{\sigma}_{pa}^{mE} \rangle + (1 - V) \langle \boldsymbol{\sigma}_M + \boldsymbol{\sigma}_{ma}^{mE} \rangle. \quad (27)$$

Then the homogenized elastic misfit residual stress in each phase  $\langle \boldsymbol{\sigma}_i^{mE} \rangle$  can be separated by subtracting  $\boldsymbol{\sigma}_M$  from  $\langle \boldsymbol{\sigma}_M + \boldsymbol{\sigma}_i^{mE} \rangle$ .

$$\langle \boldsymbol{\sigma}_i^{mE} \rangle = \langle \boldsymbol{\sigma}_M + \boldsymbol{\sigma}_i^{mE} \rangle - \boldsymbol{\sigma}_M. \quad (28)$$

The thermal misfit residual stress  $\boldsymbol{\sigma}_i^{mT}$  can be computed by constructing a boundary condition for the microscale model II via the macroscale thermal strain  $\boldsymbol{\varepsilon}_M^{th}$ .

$$\mathbf{u}_m^{II} = \boldsymbol{\varepsilon}_M^{th} \cdot \mathbf{x}_m. \quad (29)$$

With the help of the homogenization function, the homogenized thermal misfit residual stress in each phase  $\langle \boldsymbol{\sigma}_i^{mT} \rangle$  can be obtained.

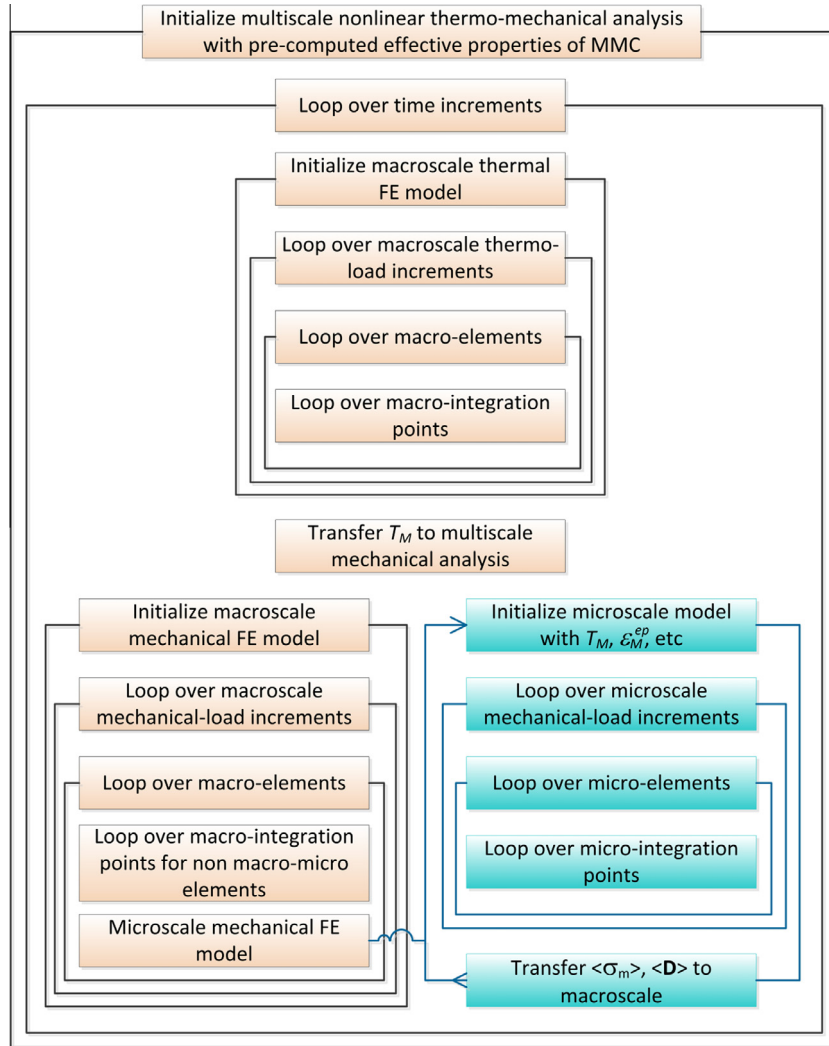


Fig. 1. Illustration of the multi-scale solution scheme for modeling the 'macro + elastic misfit' residual stresses.

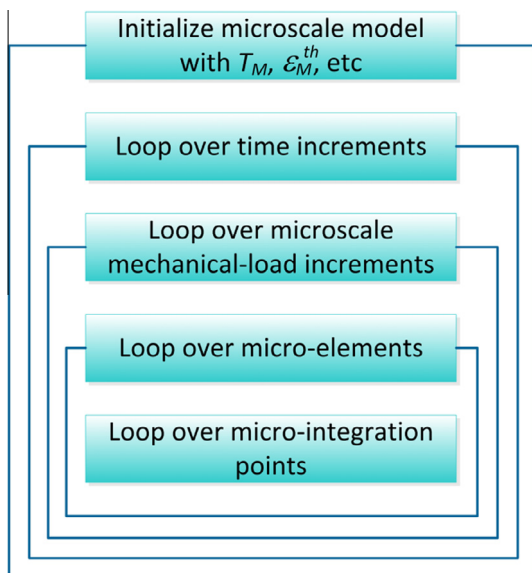


Fig. 2. Illustration of the solution scheme for modeling the thermal misfit residual stress.

The microscale stress equilibrium of  $\sigma_i^{mT}$  implies that the average of  $\sigma_i^{mT}$  over the microscale domain vanishes, which gives

$$V \langle \sigma_{pa}^{mT} \rangle + (1 - V) \langle \sigma_{ma}^{mT} \rangle = 0. \quad (30)$$

Finally, the homogenized total residual stresses  $\langle \sigma_i^{total} \rangle$  can be computed by the sum of  $\sigma_M$ ,  $\langle \sigma_i^{mE} \rangle$  and  $\langle \sigma_i^{mT} \rangle$  which is

$$\langle \sigma_i^{total} \rangle = \sigma_M + \langle \sigma_i^{mE} \rangle + \langle \sigma_i^{mT} \rangle. \quad (31)$$

Similarly, the homogenized total residual strains  $\langle \epsilon_i^{total} \rangle$  can be computed by the sum of  $\epsilon_M^e$ ,  $\langle \epsilon_i^{mE} \rangle$  and  $\langle \epsilon_i^{mT} \rangle$  which gives

$$\langle \epsilon_i^{total} \rangle = \epsilon_M^e + \langle \epsilon_i^{mE} \rangle + \langle \epsilon_i^{mT} \rangle. \quad (32)$$

### 3. Numerical computations and experiments

#### 3.1. Numerical solution framework

The model is about a *three-dimensional (3D) thermo-elastoplastic multiscale problem concerning a multiphase material*. To solve this problem, multiscale numerical method is adopted. The integration in time is discretized by the implicit finite difference (Euler-backward) method. In every time step, the spatial problem is solved

by means of multiscale numerical method based on finite element technique. All domains at both macroscale and microscale are meshed by unstructured tetrahedrons with 4-nodes using the Delaunay triangulation software TetGen [30]. Linear shape functions are used for the displacement interpolation.

The solution algorithm for solving the macro and elastic misfit residual stresses in one time step is illustrated in Fig. 1. Each time increment consists of a “macroscale thermal” part and a “multiscale mechanical” part. At the macroscale the stresses and tangential stiffness are computed via the effective constitutive model of MMC except the macro–micro points, where the stresses and tangential stiffness are computed via the microscale problem. The solution algorithm for solving the thermal misfit residual stress is illustrated in Fig. 2.

### 3.2. Material and process

As an illustration of the present multiscale model, residual stresses of a  $3\ \mu\text{m}$  17 vol.%  $\text{SiC}_p/2124\text{Al}$  composite plate quenched from 505 to  $25\ ^\circ\text{C}$  are studied.

The macroscopic geometry, coordinates, finite element meshes and the boundary faces are shown in Fig. 3. Only one eighth of the macroscopic geometry is modeled since the problem is symmetric. Eight macro–micro points are defined and their coordinates are summarized in Table 2. The eight macro–micro points approximately arranged as a line (‘a’, see Fig. 3) that is close to the measured line by the neutron diffraction reported in reference [8]. The reported experimental results [8] are taken to compare with the predicted results. The unit cell model used for the microscale simulation is shown in Fig. 4.

The temperature dependent properties of 2124Al [29,31] and SiC [32] are plotted in Fig. 5. The plastic properties of 2124Al are  $h = 0$  and  $l = 20$  which are defined in Eq. (16). The effective material properties of the  $3\ \mu\text{m}$  17 vol.%  $\text{SiC}_p/2124\text{Al}$  composite are determined by the computational homogenization technique [29].

The software MSFESL (Multi-scale finite element simulation laboratory) is developed by the present authors through object oriented techniques. The multiscale computations are carried out in MSFESL running on a ThinkStation-D20 with 2 Xeon 5690 CPUs (3.47 GHz) and 120 GB memory.

## 4. Results and discussion

### 4.1. Temperature

Fig. 6 pictures the macroscale temperature distribution at different times: the beginning (0.215 s), a short period after beginning (0.970 s) and near end of the quenching process. Obviously, a temperature gradient at different times can be observed. As one would

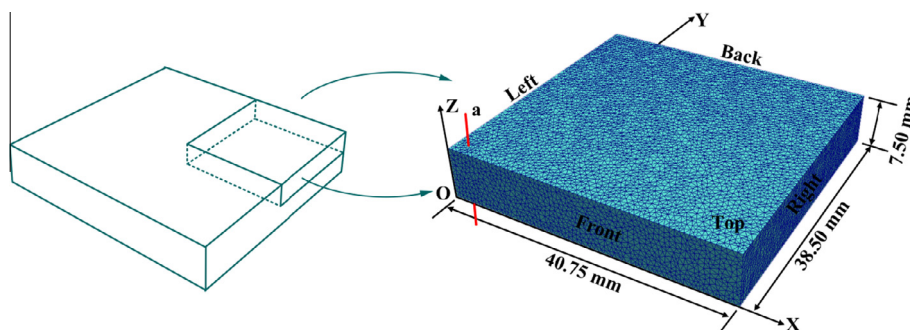


**Fig. 3.** Macro-scale symmetrical geometry model of composite plate. The macro–micro points are almost attached to the red line ‘a’ which is measured by the neutron diffraction in reference [8] so the experimental data reported in reference [8] can be used for comparison. (For interpretation of the references to color in this figure legend, the reader is referred to the web version of this article.)

**Table 2**  
Macroscopic coordinates of eight macro–micro points.

Macro–micro point	Coordinates (mm)		
	X	Y	Z
P0 <sup>a</sup>	1.90	0.40	7.38
P1	1.55	0.43	6.42
P2	2.00	0.44	5.41
P3	1.67	0.49	4.35
P4	1.63	0.43	3.12
P5	1.82	0.39	2.11
P6	1.67	0.63	0.67
P7 <sup>b</sup>	1.94	0.47	0.13

<sup>a</sup> Near the top surface of the real composite component. In the one eighth structure, P0 is also near the top boundary face.

<sup>b</sup> Near the center of the real composite component. In the one eighth structure, P7 is near the bottom boundary face.

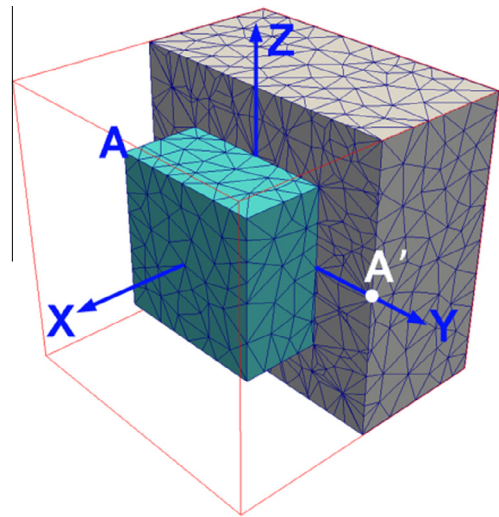


**Fig. 4.** Finite element mesh for the unit cell. Half of the matrix is transparent so that the inside particle can be seen.

expect, the temperature field is approximately isotropic in the X–Y plane of the plate except boundary regions.

The temperature history and cooling rate of P0, P3 and P7 are shown in Fig. 7. The cooling rate curves in Fig. 7(b) are obtained by differentiating the temperature curves in Fig. 7(a) with respect to time. Fig. 7(b) shows that: (i) at the beginning of quenching process, the cooling rate of the component surface (e.g. at location of P0) is higher than that of the composite inner part (e.g. at location of P3 and P7); (ii) a short period ( $\sim 0.3$  s) later, the cooling rate of

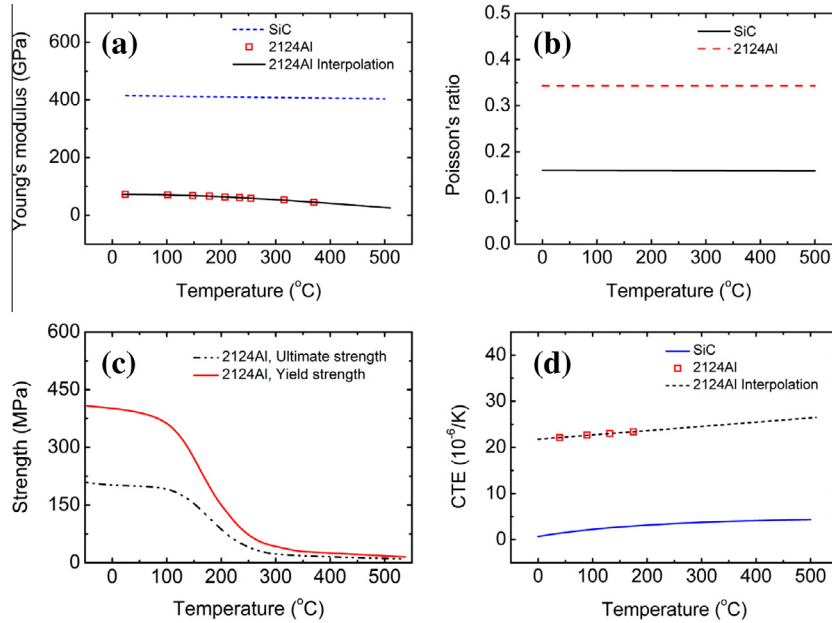


Fig. 5. Temperature dependent material properties of 2124Al [29,31] and SiC [32].

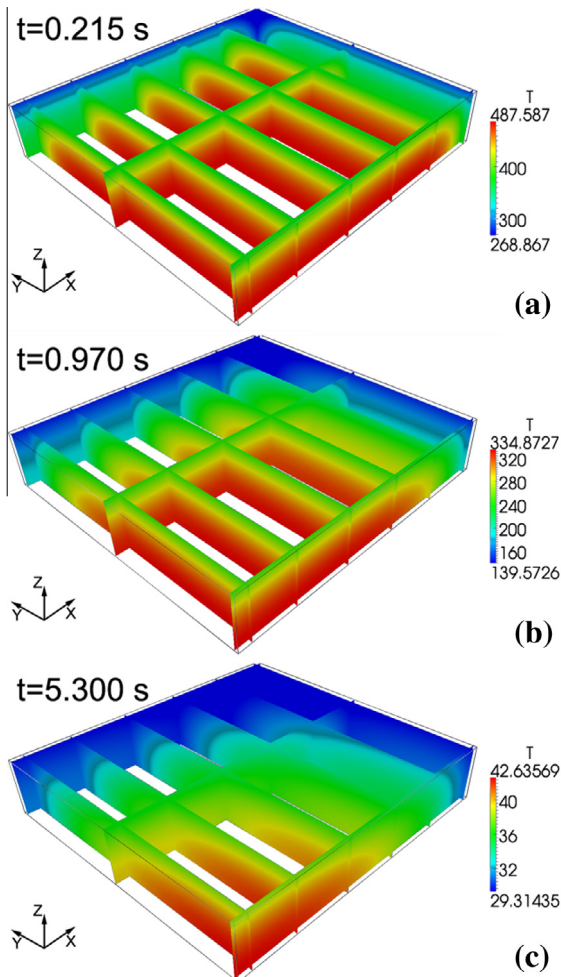


Fig. 6. Distribution of the macroscale temperature that is simulated by the macroscale model at different times during the quenching process.

the component surface is then lower than that of the composite inner part.

Figs. 6 and 7 show that both the distribution and evolution of the temperature of the plate are inhomogeneous. These characteristics of temperature will lead to inhomogeneous deformation of the MMC plate.

#### 4.2. Total residual strains and stresses

The predicted and measured total residual strains in both 2124Al and SiC are compared in Fig. 8(a) and (b). Fig. 8(a) shows that in 2124Al, the predicted total residual stress components XX and YY are very close to each other as one would expect. The predicted results are perfectly symmetrical across the half-thickness line, while the measured ones are partly asymmetrical. Both the values and the profiles of the predicted total residual strain components XX and YY agree well with the measured ones. A little difference between the predicted value of the total residual strain component ZZ and the measured one at the half-thickness location is observed.

Fig. 8(b) shows that the variation magnitude of the total residual strains in SiC is much smaller than that in 2124Al. Both the values and the profiles of the predicted total residual strain components XX and YY agree with the measured ones. The predicted total residual strain component ZZ is almost constantly 900  $\mu\epsilon$  which is lower than the measured one. The closer to the surface, the higher measured residual stress component ZZ.

The difference between the predicted and measured results may be attributed to four main factors. Firstly, the neutron measured results only reflect the residual strains of a specific  $(hkl)$  crystalline plane. In reference [8], the Al(111) reflection was used for measurements of the XX and YY components of residual strains, the Al(002) reflection was used for measurement of the ZZ component of residual strains, and the SiC(111) was used for measurement of all SiC residual strains. Differently, the present multiscale model treats the Al alloy and SiC as bulk and homogenized materials, in other words, they are molded as isotropic continuum mediums. Secondly, in real case the MMC plate has strong texture [8], while this is not considered in the multiscale simulation. Thirdly, the measured residual strains/stresses in reference

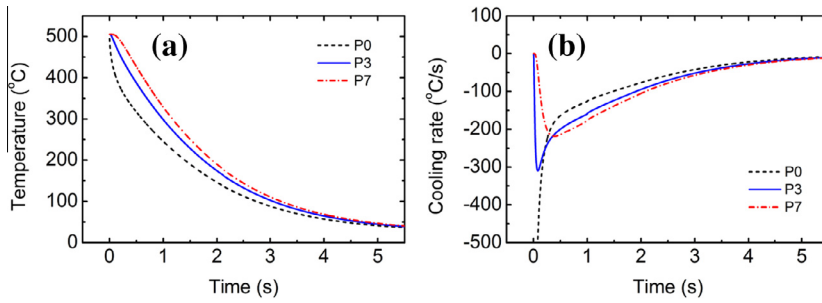


Fig. 7. Evolutions of temperature (a) and cooling rate (b) of micro-macro points P0, P3 and P7.

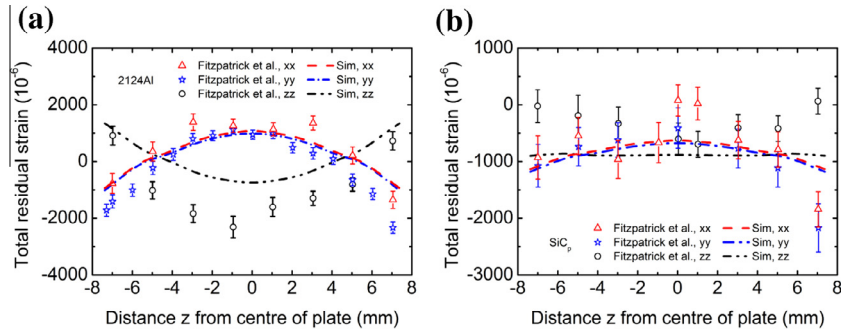


Fig. 8. Comparison between the predicted and the measured total residual strains in 2124Al and SiC.

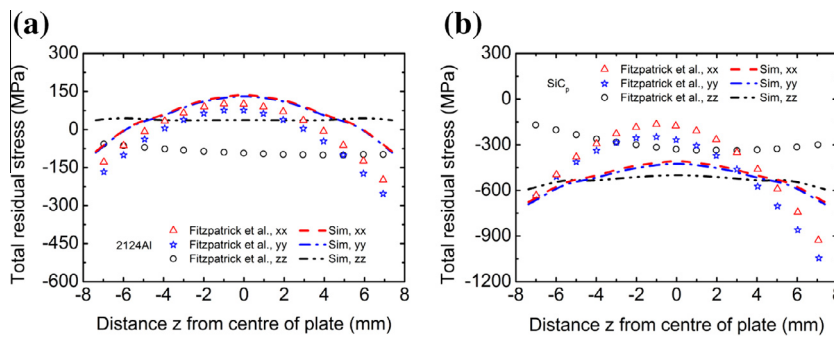


Fig. 9. Comparison between the predicted total residual stresses and the mapped residual stresses from the measured total residual strains in 2124Al and SiC.

[8] included measurement errors. According to the analysis in reference [8], all the measured total residual strain curves of 2124Al have been translated into compression with the magnitude about  $1500 \mu\epsilon$ . In order to obtain accurate measured data and assess the measurement errors, it is better to perform a measurement system analysis. Such analysis needs more measured residual strain/stress results. Fourthly, the multiscale computation involves error due to uncertainties in the input data such as the material properties of 2124Al and SiC. The computation accuracy of the multiscale model also depends on the mesh size, the time increment, the interpolation function, the element type, etc [33].

Comparison between the predicted total residual stresses in each phase and the mapped ones [8] from measured total residual strains is shown in Fig. 9. The values and profiles of the predicted and measured total residual stresses are similar. Even though, differences between the predicted and mapped total residual stresses are obvious, especially in component ZZ for both Al and SiC. For example, the predicted total residual stress  $\sigma_{Al,zz}^{total}$  is about 37 MPa, while the mapped total residual stress  $\sigma_{Al,zz}^{total}$  is about  $-75$  MPa. In another reference [5], the mapped total residual stress  $\sigma_{Al,zz}^{total}$  is about 0 MPa.

The residual stresses connect to the residual strains through the Hooke's law. Therefore, the previously mentioned reasons that cause the differences between the predicted and measured residual strains can also cause the differences between the predicted and measured residual stresses. In addition, the mapped total stresses were computed through the second order polynomial fitting functions of the measured total strains. In this way, fitting errors are introduced. Moreover, the elastic properties used in the present study to compute the residual stresses are bulk material data. Differently, those to compute the residual stresses in reference [8] were crystalline elastic properties.

#### 4.3. Macro residual strains and stresses

In Fig. 10, the predicted macro residual stresses via both the macroscale model and the microscale model I are compared with the reported measurement results [8], which are mapped from the measured residual strains with the help of the Eshelby model. As expected, the computed macro residual stresses are the same as those homogenized from the microscale model despite some numerical error. This verifies that  $\langle \sigma_M + \sigma_i^{mE} \rangle = 0$ , in other words,

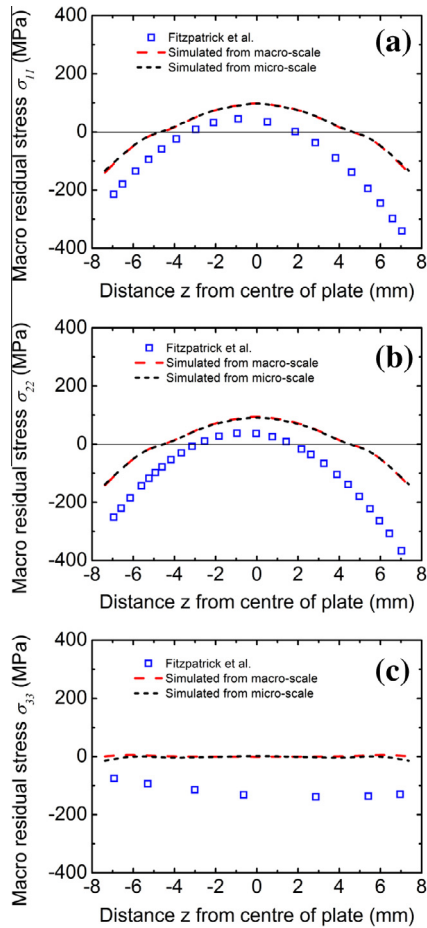


**Fig. 10.** Comparison between the multiscale predicted macro residual stresses and the separated macro residual stresses via Eshelby model. The “simulated from macroscale” denotes that the macro residual stresses are computed directly from the macroscale problem. The “simulated from macroscale” denotes that the macro residual stresses are homogenized from microscale model I.

Eq. (27) holds. This confirms that the numerical accuracy of the multiscale computation is quite good. Furthermore, the predicted macro residual stress components XX, YY and ZZ integrate to zero across the thickness of plate. The variation profile of the predicted macro residual stress components XX and YY is close to a second order polynomial curve. However, according to reference [8], the reported results appeared to be net compression due to the measure problem with the  $d_0$  parameter.

The macro residual stress distribution is shown in Fig. 11. It can be seen that the field of the macro residual stress component XX is more or less a 90° rotation of that of the component YY. The results also confirm that all three components of the macro residual stress in the X–Y plane are approximately isotropic except the near boundary regions where significant boundary effects exist.

The heterogeneous distribution and evolution of the macro temperature lead to inhomogeneous deformation across the whole macro domain. As a result, internal stress presented. In reality, when the stress in the metal matrix reaches its yield stress plastic deformation occurs in the metal matrix. However, the MMC is modeled as a (virtual) homogeneous material at the macroscale. Hence, when the stress in the homogenized MMC reaches the effective yield stress, plastic flow starts in the homogeneous material.

Fig. 12 shows that the maximum APS is ~0.0025. This value reflects the level of the plastic deformation that is caused by the inhomogeneities of the macro temperature distribution and

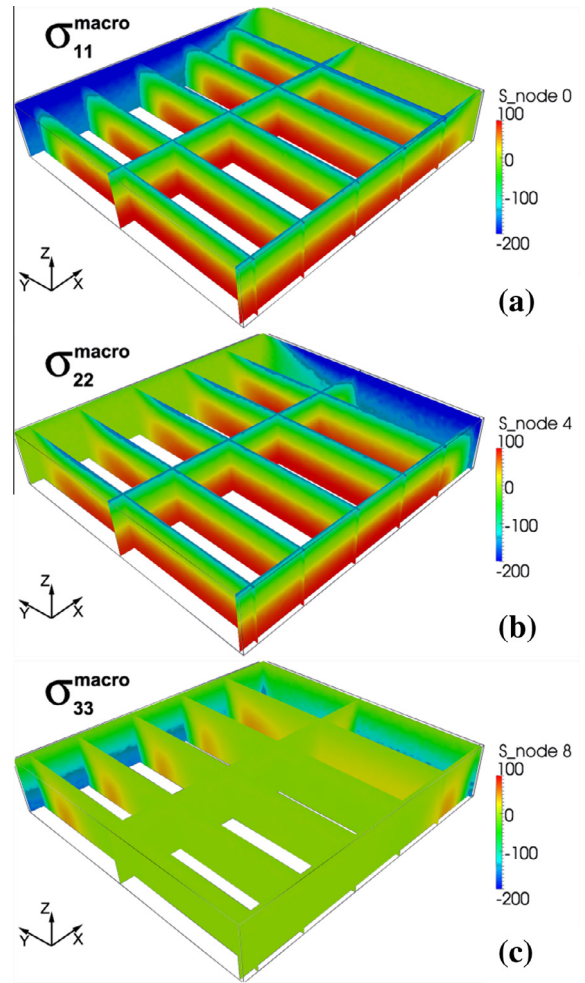


**Fig. 11.** Distribution of the macro residual stresses that is computed by the macroscale model.

evolution. The plastic deformation caused by the misfit of the elastic properties or the CTE between the reinforcing particles and the metal matrix will be considered in the microscale model rather than in the macroscale model.

It is worth noting that from the atomic perspective, plastic deformation of the polycrystalline metals or alloys is a consequence of the comparable distortion of the individual grains by means of dislocation slip. During the continuous plastic flow different microscale processes predominate. Besides, plastic deformation is a history dependent physical process, but not a thermodynamic state function. Although the constitutive equations can reasonably capture the strain–stress curves, they describe the elasto-plastic deformation in a phenomenological way rather than in a physically satisfactory way. Hence, the APS (e.g. shown in Fig. 12) that reflect the level of plastic deformation is not uniquely related to the dislocation structure of the material and does not have definite physical significance [34].

4.4. Elastic misfit residual strains and stresses

The predicted elastic misfit residual stresses in both 2124Al and SiC are plotted in Fig. 13, together with the mapped ones determined from reference [8]. It can be seen that the predicted components XX and YY approximately agree with the mapped ones. However, the variation trend of the mapped component ZZ is opposite to that of the predicted one. In addition, it can be seen

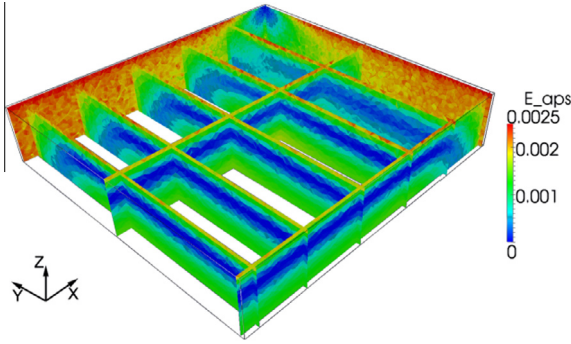


Fig. 12. Distribution of the accumulated plastic strain that is calculated by the macroscale model.

that the variation amplitudes of the elastic misfit residual stresses are much smaller than those of the total residual stresses. This can also be explained by the analytical equation proposed in reference [8], i.e., the elastic misfit residual stress component XX in the metal matrix is [8]

$$\langle \sigma_{xx,ma}^{mE} \rangle = -0.100\sigma_{M,xx} + 0.0265\sigma_{M,yy} + 0.0265\sigma_{M,zz}. \quad (33)$$

Because  $\sigma_{xx}^{macro} \approx \sigma_{yy}^{macro}$ , and  $\sigma_{zz}^{macro} \approx 0$ , as shown in Fig. 10,  $\langle \sigma_{xx,ma}^{mE} \rangle$  then approximates

$$\langle \sigma_{xx,ma}^{mE} \rangle \approx (-0.100 + 0.0265)\sigma_{M,xx} = -0.0735\sigma_{M,xx}. \quad (34)$$

The 3D elastic misfit residual stress fields at different macro-micro points (in other words, different macroscale locations) are pictured in Fig. 14. As shown in Fig. 14(a)–(c), at P0, for all three components XX, YY and ZZ, the metal matrix mainly maintains tensile elastic misfit residual stress (the red and yellow areas). However, obvious compressive elastic misfit residual stress can also be seen in some parts (the blue part). The particle undergoes pure compressive elastic misfit residual stress. At P3, as shown in Fig. 14(d)–(f), all three components XX, YY and ZZ approximate to zero. This is because the macro residual stress at the location ( $\pm 4.35$  mm away from the center of the plate along the thickness, i.e. Z, direction) of P3 is near zero as shown in Fig. 10. At P7 (i.e. the location of  $\pm 0.13$  mm away from the center of the plate along the thickness direction), as shown in Fig. 14(g)–(i), the metal matrix contains both compressive and tensile elastic misfit residual stresses. The area of the compressive ones is larger than that of the tensile ones. Hence, the metal matrix apparently maintains compressive elastic misfit residual stress.

The elastic misfit residual stresses are accompanied by the macro residual stresses. Therefore, the macro and elastic misfit residual stresses, i.e.  $\sigma_M + \sigma_i^{mE}$ , are calculated together in microscale model I. If the von-Mises equivalent stress in the metal

matrix exceeds its yield strength, plastic deformation occurs. Fig. 15 shows the corresponding APS fields at different macro-micro points, P0, P3 and P7. It should be mentioned here that these APS fields are caused by the macroscale temperature gradient and the misfit of elastic properties, especially the elastic modulus. It can be seen that the metal matrix at P0 experiences the maximum level of plastic deformation, while at P3 the metal almost has no plastic deformation.

#### 4.5. Thermal misfit residual strains and stresses

Fig. 16 compares the predicted thermal misfit residual stresses from the microscale model II and the mapped ones with the help of the Eshelby model [8]. As expected, the predicted thermal misfit residual stresses are hydrostatic, i.e. the three principal directions have the same value. The predicted thermal misfit residual stresses in the metal matrix (about 40.0 MPa) and the mapped ones agree well with each other. However, the predicted ones in particles (about  $-458.0$  MPa) and the mapped ones differ. The mapped thermal misfit residual stresses were not hydrostatic probably due to errors from measurement and data process [8].

One may expect that the stress equilibrium of the thermal misfit residual stresses over the microscale domain equals to zero according to Eq. (30). Actually,  $0.17 \times (-458) + (1.0 - 0.17) \times 40 \text{ MPa} = -44.66 \text{ MPa}$ , which is undesirable non-zero. Meanwhile, as shown in Fig. 17, concerning each component of the thermal misfit residual stress, a part of the metal matrix exhibits compressive stress. For example, concerning the thermal misfit residual stress component XX, a part of area with compressive stress is present in the metal matrix along the X-axis direction.

The reason for this may be due to the computational error introduced by the linear displacement boundary condition (see Eq. (29)). In the multiscale mechanics theory, in order to obey the Hill' condition [35]

$$\begin{aligned} \langle \sigma_m : \epsilon_m \rangle - \langle \sigma_m \rangle : \langle \epsilon_m \rangle \\ = \frac{1}{V_m} \int_{\partial V_m} (\mathbf{u}_m - \langle \epsilon_m \rangle \cdot \mathbf{x}) \cdot (\mathbf{t}_m - \langle \sigma_m \rangle \cdot \mathbf{n}) dS_m = 0, \end{aligned} \quad (35)$$

two basic types of boundaries are frequently used: the KUBC as shown by Eq. (10), and the static uniform boundary conditions (SUBC) [36]. However, in the strict sense, the KUBC is a strong boundary condition. There is no reason to assume that the RVE boundaries will remain flat. When the boundaries are assumed to be flat, the KUBC impose undesirable constraints, for example, the situation occurs here is that the KUBC cannot guaranty that  $\langle \sigma_m \rangle = 0$ , in other words,  $\mathbf{t}_m \neq 0$ . The SUBC may improve the accuracy and help to solve this problem because  $\mathbf{t}_m$  can be set to a zero vector in the SUBC. This is a subject of our current work.

Concerning the influence of the KUBC on the multiscale computation accuracy, one might worry that the KUBC may also affect the

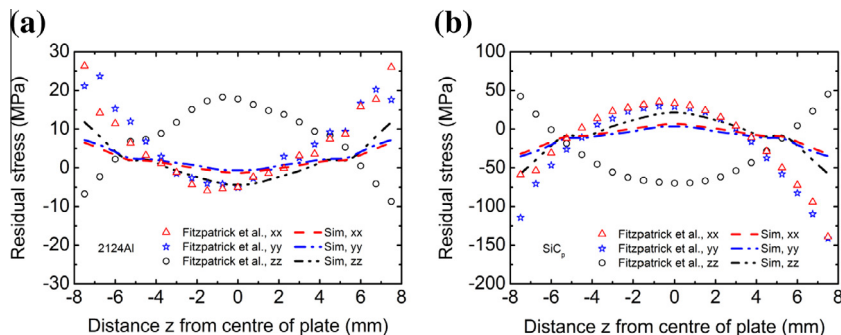
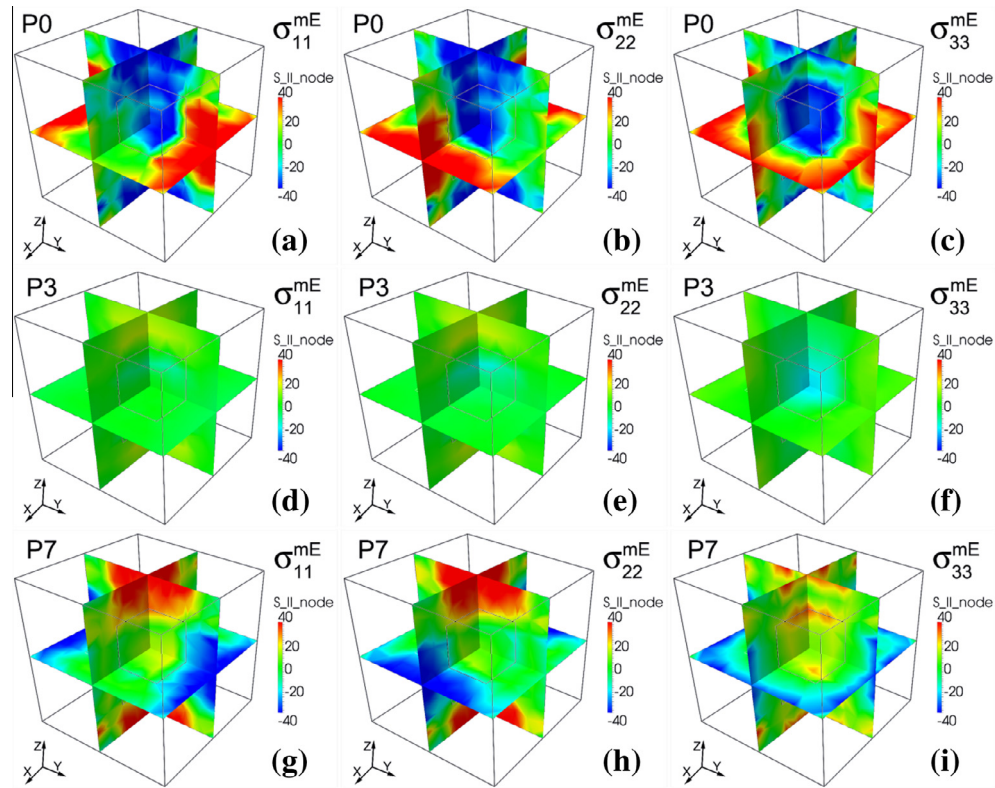
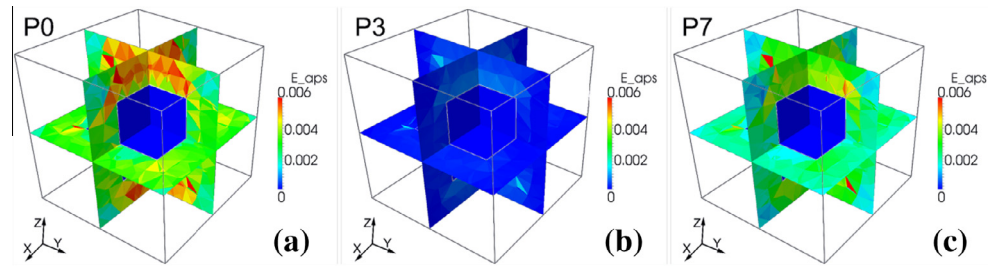


Fig. 13. Comparison between the predicted elastic misfit residual stresses via Microstructure model I and the determined elastic misfit residual stresses via Eshelby model in 2124Al and SiC.



**Fig. 14.** The 3D elastic misfit residual stress fields: (a), (b), (c) at micro–macro point P0; (d), (e), (f) at micro–macro point P3; (g), (h), (i) at micro–macro point P7. (For interpretation of the references to color in this figure legend, the reader is referred to the web version of this article.)



**Fig. 15.** The 3D accumulated plastic strain fields at different micro–macro points computed by microscale model I.

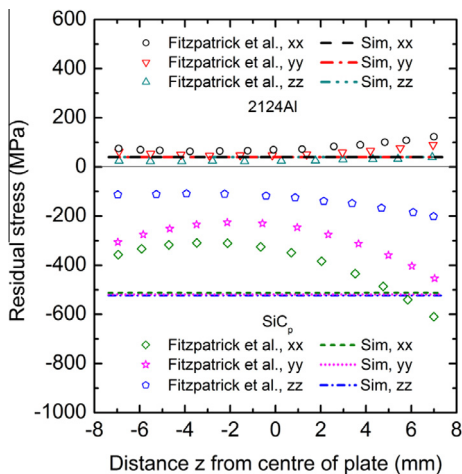


**Fig. 16.** Comparison between the predicted thermal misfit residual stresses via Microstructure model II and the separated thermal misfit residual stresses via Eshelby model in 2124Al and SiC.

computation accuracy of the macro and elastic misfit residual stresses. The computation results dissolve this worry, because as indicated by the results in Fig. 10, Eq. (27) holds.

The APS field caused by the thermal misfit is shown in Fig. 18. It can be seen that the metal matrix is more or less divided into two parts: the inner part and the outer part. In the inner part near to the matrix/particle interface large plastic deformation occurs, while in the outer part near the boundary the plastic deformation drops to a small value. Such a distribution differs from the image in Fig. 15, where the APS that is caused by the macroscale temperature gradient and the elastic misfit is more uniformly distributed in the whole part of the metal matrix. The large plastic deformation in the inner part near to the matrix/particle interface releases the residual stress significantly and promotes the damage near to the matrix/particle interface.

#### 4.6. Applications and future developments of the present multiscale model

In the present multiscale model, all phases in heterogeneous materials are modeled as general elasto-plastic materials. In this

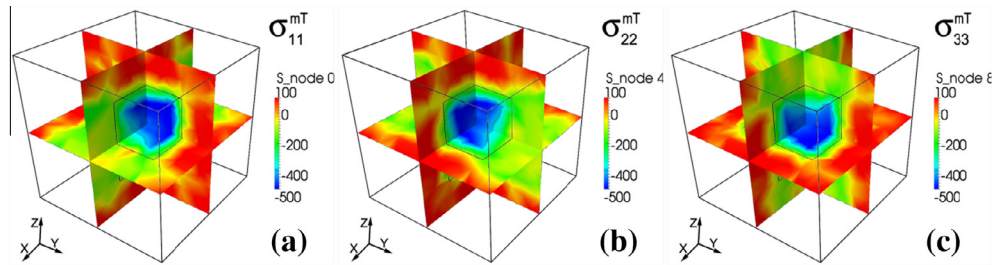


Fig. 17. The distribution of the thermal misfit residual stress computed by microscale model II.

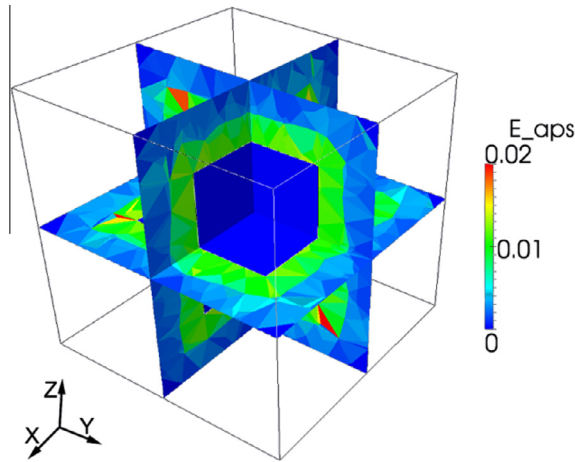


Fig. 18. The distribution of the accumulated plastic strain computed by microscale model II.

way, in addition to the metal matrix composites, other heterogeneous materials, for instance, the dual-phase steel [37] could be also included in this framework. For phases that only show an elastic deformation, the yield strength can then be set to a large value as done in the present work. Regarding the fiber or whisker reinforced metal matrix composites, the effective constitutive model should consider the anisotropic behaviors of thermal and mechanical properties. For example, the Hill's yield criterion could be considered.

The future development in predicting the residual stresses in heterogeneous materials at least includes: (i) predicting the origins of residual stress during material forming process (for this case, extension of the present model to the finite deformation framework is required) and welding; (ii) predicting the residual stress evolution during in-service and failure processes. These require a lot of works to do. Integrated finite element simulation technique may be a proper method to transfer the residual stresses to the model about the in-service and failure processes. Furthermore, in order to obtain more accurate results and take account of the real microstructure attributes, simulated realistic microstructures or scanned real microstructures by means of micro-CT technique should be employed. In this case, the computational efficiency should also be improved.

## 5. Conclusions

1. This is the first attempt to develop a 3D multiphysical multi-scale model to study the residual stresses in multiphase materials under the hybrid-semiconcurrent multiscale framework. As an illustration, the quenching residual stresses in SiC<sub>p</sub>/2124Al composites are modeled. The total residual stresses are then separated into the macro, elastic misfit and thermal

misfit residual stresses. The present model provides a new tool to gain a deep insight into the residual stresses in multiphase materials.

2. The model shows very encouraging results which coincide with reported experimental data very well. The predicted total residual strains in the metal matrix and the reinforcing particles agree very well with the reported measured ones. The predicted total, macro, elastic misfit and thermal misfit residual stresses agree reasonably well with the reported experimental ones.

## Acknowledgments

The authors gratefully acknowledge the support of the National Natural Science Foundation of China under Grant No. 51401219 and the National Basic Research Program of China under Grant No. 2012CB619600.

## References

- [1] Durieux S, Buffiere JY, Lormand G, Rapoport A, Vincent A. Enhanced plasticity in metal matrix composites during thermal cycling under load. *Mater Sci Eng A* 1997;234:953–7.
- [2] Bussu G, Irving PE. The role of residual stress and heat affected zone properties on fatigue crack propagation in friction stir welded 2024-T351 aluminium joints. *Int J Fatigue* 2003;25:77–88.
- [3] John R, Jata KV, Sadananda K. Residual stress effects on near-threshold fatigue crack growth in friction stir welds in aerospace alloys. *Int J Fatigue* 2003;25:939–48.
- [4] Fernandez R, Bruno G, Gonzalez-Doncel G. Correlation between residual stresses and the strength differential effect in PM 6061Al-15 vol% SiCw composites: experiments, models and predictions. *Acta Mater* 2004;52:5471–83.
- [5] Fitzpatrick ME, Hutchings MT, King JE, Knowles DM, Withers PJ. Effect of thermal residual stresses on fatigue crack opening and propagation behavior in an Al/SiC<sub>p</sub> metal matrix composite. *Metall Mater Trans A* 1995;26:3191–8.
- [6] Knowles DM, King JE. Influence of macroscopic residual-stress fields on fatigue crack-growth measurement in sic particulate reinforced 8090 aluminum-alloy. *Mater Sci Technol* 1991;7:1015–20.
- [7] Withers PJ. Residual stress and its role in failure. *Rep Prog Phys* 2007;70:2211–64.
- [8] Fitzpatrick ME, Hutchings MT, Withers PJ. Separation of macroscopic, elastic mismatch and thermal expansion misfit stresses in metal matrix composite quenched plates from neutron diffraction measurements. *Acta Mater* 1997;45:4867–76.
- [9] Analysis of residual stress by diffraction using neutron and synchrotron radiation. London: Taylor & Francis; 2003.
- [10] Ganguly S, Edwards L, Fitzpatrick ME. Problems in using a comb sample as a stress-free reference for the determination of welding residual stress by diffraction. *Mater Sci Eng A* 2011;528:1226–32.
- [11] Bruno G, Fernandez R, Gonzalez-Doncel G. Gauge volume effects in residual stress determination by neutron diffraction: the strength differential effect in metal matrix composites. *Mater Sci Eng A* 2006;437:100–8.
- [12] Wimporoy RC, Ohms C, Hofmann M, Schneider R, Youtsos AG. Statistical analysis of residual stress determinations using neutron diffraction. *Int J Press Vessels Pip* 2009;86:48–62.
- [13] Povirk GL, Stout MG, Bourke M, Goldstone JA, Lawson AC, Lovato M, et al. Thermally and mechanically induced residual strains in Al–SiC composites. *Acta Metall Mater* 1992;40:2391–412.
- [14] Ho S, Saigal A. Three-dimensional modelling of thermal residual stresses and mechanical behavior of cast SiC/Al particulate composites. *Acta Metall Mater* 1994;42:3253–62.
- [15] Schmauder S, Weber U, Sopha E. Computational mechanics of heterogeneous materials–influence of residual stresses. *Comput Mater Sci* 2003;26:142–53.

- [16] Bouafia F, Serier B, Bouiadjra BAB. Finite element analysis of the thermal residual stresses of SiC particle reinforced aluminum composite. *Comput Mater Sci* 2012;54:195–203.
- [17] Davis LC, Allison JE. Residual-stresses and their effects on deformation in particle-reinforced metal-matrix composites. *Metall Trans A* 1993;24:2487–96.
- [18] Llorca J, Gonzalez C, Molina-Aldareguia JM, Segurado J, Seltzer R, Sket F, et al. Multiscale modeling of composite materials: a roadmap towards virtual testing. *Adv Mater* 2011;23:5130–47.
- [19] Ghosh S, Lee K, Moorthy S. Two scale analysis of heterogeneous elastic-plastic materials with asymptotic homogenization and Voronoi cell finite element model. *Comput Methods Appl M* 1996;132:63–116.
- [20] Ghosh S, Lee K, Raghavan P. A multi-level computational model for multi-scale damage analysis in composite and porous materials. *Int J Solids Struct* 2001;38:2335–85.
- [21] Özdemir I, Brekelmans WAM, Geers MGD. FE<sup>2</sup> computational homogenization for the thermo-mechanical analysis of heterogeneous solids. *Comput Methods Appl Mech Eng* 2008;198:602–13.
- [22] Golanski D, Terada K, Kikuchi N. Macro and micro scale modeling of thermal residual stresses in metal matrix composite surface layers by the homogenization method. *Comput Mech* 1997;19:188–202.
- [23] Weinan E, Engquist B, Li XT, Ren WQ, Vanden-Eijnden E. Heterogeneous multiscale methods: a review. *Commun Comput Phys* 2007;2:367–450.
- [24] Belytschko T, Song JH. Coarse-graining of multiscale crack propagation. *Int J Numer Methods Eng* 2010;81:537–63.
- [25] Feyel F. Application du calcul parallèle aux modèles à grand nombre de variables internes [Thèse de doctorat]: école Nationale Supérieure des Mines de Paris; 1998.
- [26] Feyel F, Chaboche JL. FE<sup>2</sup> multiscale approach for modelling the elastoviscoplastic behaviour of long fibre SiC/Ti composite materials. *Comput Methods Appl M* 2000;183:309–30.
- [27] Laurence B. Homogenization of elasto-(visco)plastic composites: history-dependent incremental and variational approaches [PhD Thesis]: université catholique de Louvain; 2011.
- [28] Voce E. A practical strain-hardening function. *Metallurgica* 1955;51:219–26.
- [29] Zhang XX, Xiao BL, Andrä H, Ma ZY. Homogenization of the average thermo-elastoplastic properties of particle reinforced metal matrix composites: the minimum representative volume element size. *Compos Struct* 2014;113:459–68.
- [30] Si H. TetGen a quality tetrahedral mesh generator and three-dimensional delaunay triangulator. 1.4 ed.; 2006.
- [31] Aerospace structural metals database <<https://cindasdata.com/Applications/ASMD/?subaction=reload%3Amcode&mname=2124&mcode=3221>>.
- [32] Munro RG. Material properties of a sintered alpha-SiC. *J Phys Chem Refer Data* 1997;26:1195–203.
- [33] Zienkiewicz OC, Taylor RL. Finite element method: the basis. 5th ed. Oxford: Butterworth-Heinemann; 2000.
- [34] Meyers MA, Chawla KK. Mechanical behavior of materials. 2nd ed. Cambridge: Cambridge University Press; 2008.
- [35] Hill R. Elastic properties of reinforced solids: some theoretical principles. *J Mech Phys Solids* 1963;11:357–72.
- [36] Hazanov S. Hill condition and overall properties of composites. *Arch Appl Mech* 1998;68:385–94.
- [37] Sun X, Choi KS, Liu WN, Khaleel MA. Predicting failure modes and ductility of dual phase steels using plastic strain localization. *Int J Plast* 2009;25:1888–909.